Fabrication of a near-infrared fluorescence-emitting SiO2-AuZnFeSeS quantum dots-molecularly imprinted polymer nanocomposite for the ultrasensitive fluorescence detection of levamisole

Adegoke, Oluwasesan; Zolotovskaya, Svetlana A.; Abdolvand, Amin; Nic Daeid, Niamh

Published in:
Colloids and Surfaces A: Physicochemical and Engineering Aspects

DOI:
10.1016/j.colsurfa.2022.129013

Publication date:
2022

Colloids and Surfaces A: Physicochemical and Engineering Aspects 646 (2022) 129013

Contents lists available at ScienceDirect

Colloids and Surfaces A: Physicochemical and Engineering Aspects

journal homepage: www.elsevier.com/locate/colsurfa

Fabrication of a near-infrared fluorescence-emitting SiO_2-AuZnFeSeS quantum dots-molecularly imprinted polymer nanocomposite for the ultrasensitive fluorescence detection of levamisole

Oluwasesan Adegoke [a,*], Svetlana Zolotovskaya [b], Amin Abdolvand [b], Niamh Nic Daeid [a]

[a] Leverhulme Research Centre for Forensic Science, University of Dundee, Dundee DD1 4HN, UK
[b] Materials Science & Engineering Research Cluster, School of Science & Engineering, University of Dundee, Dundee DD1 4HN, UK

HIGHLIGHTS

- Novel SiO_2-encapsulated AuZnFeSeS alloyed QDs was synthesized and characterized.
- An MIP shell specific for levamisole was coated around the AuZnFeSeS QDs to form a AuZnFeSeS QDs@nanocomposite.
- Levamisole was ultrasensitively detected and was selectively against other tested drugs.
- The AuZnFeSeS QDs@MIP nanocomposite probe was used to detect levamisole in mixed drug sample.

GRAPHICAL ABSTRACT

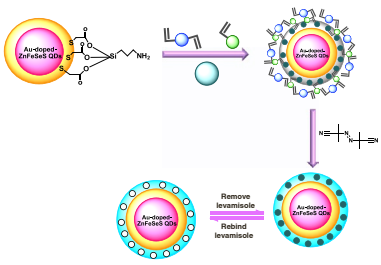

ARTICLE INFO

Keywords:
Molecularly imprinted polymer
Quantum dots
Fluorescence
Detection
Nanocomposite

ABSTRACT

Levamisole is an anthelminthic drug that is usually used as a cutting agent to lace illicit cocaine samples and has been classified as a dangerous substance. In this work, we report on the fabrication of a novel fluorescence sensor for levamisole using AuZnFeSeS alloyed quantum dots (QDs)-molecularly imprinted polymer (MIP) nanocomposite. Firstly, organic-phased AuZnFeSeS QDs were synthesized via the organometallic hot-injection pyrolysis of metal precursors, surfactants, and organic ligands. Silica (SiO_2) was then encapsulated on the QDs surface to render it compact, stable, and biocompatible. Via a free radical polymerization approach, a robust MIP shell templated with levamisole was coated around the SiO_2-AuZnFeSeS QDs surface to form a AuZnFeSeS QDs@MIP core/shell nanocomposite. Passivation of the SiO_2-AuZnFeSeS QDs core surface with the MIP shell led to radiative exciton recombination process, whereby the QDs fluorescence was enhanced. Interestingly, the SiO_2-AuZnFeSeS QDs was characterized by rod-shaped and spherical-shaped particle morphology. Under optimum conditions, the fluorescence of the AuZnFeSeS QDs@MIP nanocomposite was quenched in the presence of levamisole and was selective against other tested drugs. Quantitative detection was achieved in the concentration range of 0.5 – 100 μM with a limit of detection of 0.05 μM (47.4 nM). Validation of the MIP-levamisole affinity was demonstrated by the superior sensitivity of the AuZnFeSeS QDs@MIP over the AuZnFeSeS QDs@NIP (non-templated material). Levamisole was successfully detected in a mixed drug sample containing cocaine with satisfactory analytical recoveries. This work is the first reported use of a cadmium-free quintenary alloyed QDs@MIP nanocomposite fluorescence detection system for levamisole.

* Correspondence to: Leverhulme Research Centre for Forensic Science, School of Science & Engineering, University of Dundee, Dundee DD1 4GH, UK.
E-mail address: UKo.adegoke@dundee.ac.uk (O. Adegoke).

https://doi.org/10.1016/j.colsurfa.2022.129013
Received 26 January 2022; Received in revised form 11 April 2022; Accepted 12 April 2022
Available online 14 April 2022

1. Introduction

Levamisole, (IUPAC name: 2,3,5,6-tetrahydro-6-phenylimidazo(2,1-b)thiazole) is an anthelminthic drug that was once used to treat humans infected with parasitic worm. It was withdrawn from the Canadian and U.S. markets in 2003 and 1999, due to the availability of better medications and the risk of adverse side effects arising from the drug use [1]. News media outlets such as the Time Magazine, government agencies and scientific publications have alerted the general public, physicians, and health officials about the possible life-threatening consequences of cocaine laced with levamisole [2–4]. A classic example of such public alert warning was issued in September 2009 by the Department of Health and Human Services Substance Abuse and Mental Health Services Administration, US, that a very dangerous substance known as levamisole was showing up with alarming frequency in crack cocaine and illicit cocaine powder and can induce agranulocytosis, a problem associated with low number of white blood cells [5].

According to reports from the Advisory Council on the Misuse of Drugs (ACMD), UK, levamisole was considered the most detected active cutting agent in seized drugs between 2012 and 2013 [6]. Also, estimates from the Drug Enforcement Agency (DEA) indicate that 80% of seized cocaine in the U.S. also contains levamisole [5]. Speculation about the addition of levamisole to cocaine centers around two main theories. The first is that levamisole is cheap, easily accessible, and of similar physicochemical properties to cocaine. As a consequence, it would be considered an obvious material to use as a bulking agent for cocaine with the aim of generating increased profit. The second conception centres around the believe that levamisole is able to modify the pharmacological properties of cocaine [5].

To date, there are several developed sensing methods for levamisole recognition. Examples include the use of chromatographic analytical techniques such as gas chromatography (GC), high performance liquid chromatography (HPLC), liquid chromatography-thermospray mass spectrometry, and GC-electron impact mass spectrometry [6–9]. Although, rapid detection of levamisole has been achieved using these chromatographic techniques, several stages of extraction processes are generally required prior to analysis. Also, prolonged analysis time, inefficient sample throughput, and the need for highly experienced instrumental analyst to operate the instruments, limits the use of chromatographic techniques for routine levamisole analysis. Immuno-based sensing methods have also been reported for levamisole screening [10, 11]. However, the use of antibodies as bioreceptors in sensing applications comes with its own limitations such as high cost of production, limited stability, and high susceptibility to false positive or false negative signals. Electrochemical sensing of levamisole using molecularly imprinted polymers (MIPs) have also been reported [12]. Although, the electrochemical MIP work showed some promise with regard to selectivity against substances of similar structure to levamisole, there was however, no selectivity study involving a cocaine sample which also contained levamisole or the direct detection of levamisole in a cocaine sample. In addition, the sensitivity of the assay was limited by the instrument electrode substate support. It is therefore of interest to develop highly sensitive, selective, and robust sensing systems for Levamisole.

Due to the need to circumvent the limitations of conventional analytical sensing methods, the use of artificial receptors in chemical assays have drawn significant interest [13–15]. Wulff and Sarhan where the first to developed molecular imprinting as a form of artificial receptor back in 1972 as they were able to establish a suitable synthetic approach for its manufacture [16]. MIPs are best described as synthetic analogue mimics to the traditional antigen-antibody interaction binding system. As such, the mode of operation mimics a “lock and key” principle to selectively rebind the templated analyte of interest [17]. MIPs are generally produced when a prepolymer is polymerized in the presence of a template molecule. Negative charges in the targeted template molecule will generally orient themselves towards positive charges in the polymer matrix via noncovalent interactions such as hydrogen bonding, π-π, hydrophobic and ionic interactions [17]. Due to the ease of template removal, the noncovalent interaction between the template and cavity is much more favoured. In principle, when the template molecule is removed from the polymer matrix, it leaves a target-specific cavity of a specific size and shape which is readily available for rebinding. The MIP is then exposed to the template sample in a rebinding process to aid selective detection of the target analyte.

Precipitation polymerization, emulsion polymerization, high dilution polymerization, core/shell approaches, surface-imprinted materials and solid-phase synthesis, are examples of synthetic methods used to produce MIPs [18–36]. In order to achieve robust assay results including enhanced sensitivity, core/shell MIP approaches has been used as the main fabrication strategy. This involves coating the MIP shell around core particles such as silica [37], iron oxide nanoparticles (NPs) [38], semiconductor quantum dots (QDs) [39–41], carbon dots [42], plasmonic NPs [43] and several hybrid-based nanomaterials [44]. Particularly, fluorescent-based MIP nanocomposites have found wide applications for the detection of explosives, pesticides, drugs, peptides, and proteins [45]. Amongst the various fluorophores that have been used in MIP fluorescence sensing applications, QDs nanocrystals, which exhibits size confinement on the nanoscale in a three-dimensional fashion, have drawn considerable interest [46]. QDs are generally more photostable, size-dependent, and exhibits narrower emission and broader absorption spectra than organic-fluorophore dyes and other nanofluorophores such as carbon dots and graphene QDs [47]. However, most of the semiconductor QDs that have been used in the development of QDs@MIP fluorescence sensor systems are mainly composed of the toxic cadmium ion [39]. Hence, to avoid the use of cadmium-based QDs, environmentally friendly metal chalcogenides were chosen in this work. To date, no QDs-MIP nanocomposite fluorescence sensor has been reported for levamisole detection. The only report on the use of MIP for levamisole detection is the work by Sadeghi et al., who used direct electrochemistry with the electrode as a substrate to anchor the MIP [12].

In this work, we report for the first time on the development of a novel AuZnFeSeS QDs@MIP core/shell nanocomposite fluorescence sensor system for levamisole. Recently, we have previously reported on the development of an environmentally friendly amphiphilic polymer-coated AuFeZnSe QDs for heavy metal fluorescence sensing [48]. In this work, S was embedded into the AuFeZnSe QDs structure to form a new near-infrared (NIR) fluorescence-emitting AuZnFeSeS QDs system with the aim of generating new optical properties. The advantages of NIR fluorescence QDs are the significant elimination of Rayleigh scattering, deeper tissue penetration and the generation of non-invasiveness [49]. The NIR fluorescence-emitting AuZnFeSeS QDs were first synthesized via the organometallic hot-injection synthetic route and thereafter surface-coated with silica (SiO_2) to render the QDs biocompatible, stable, and compact. Using a free radical polymerization approach, the MIP shell was overcoated around the SiO_2-AuZnFeSeS QDs core surface in the presence of the targeted levamisole template Specifically, the synthesized SiO_2-AuZnFeSeS QDs was used as a core support for the MIP shell and as a fluorescence signal reporter for levamisole recognition. A non-imprinting SiO_2-AuZnFeSeS QDs@NIP was also fabricated to validate the sensitivity of the AuZnFeSeS QDs@MIP towards levamisole recognition. An ultrasensitive and selective fluorescence sensor system was developed for levamisole using the AuZnFeSeS QDs@MIP nanocomposite system in water and in mixed drug system.

2. Experimental

2.1. Chemicals

Ethylene glycol dimethacrylate (EGDMA), acrylamide, levamisole hydrochloride, cocaine hydrochloride, methamphetamine hydrochloride (MAMP), amphetamine hydrochloride (AMP), (3-aminopropyl) triethoxysilane (APTES), iron (III) chloride ($FeCl_3$), oleylamine,

hexadecylamine (HDA), selenium (Se), sodium oleate, acrylamide, 2,2′-azobis(2-methylpropionitrile) (AIBN), sodium acetate (NaAc), tris (hydroxymethyl)aminomethane acetate salt (Trizma® Ac), trioctylyphosphine oxide (TOPO), trioctylyphosphine (TOP), oleic acid, sulphur, potassium thiocyanate (KSCN), borax, tetraethyl orthosilicate (TEOS), 2,2′-azobis(2-methylpropionitrile), zinc chloride and octadecene were purchased from Merck. Myristic acid, 2-(n-morpholino) ethanesulfonic acid (MES), trisodium citrate, potassium acetate (Kac) and gold (III) chloride trihydrate ($HAuCl_4.3\ H_2O$) were purchased from Thermo Fisher. 3,4-Methylenedioxymetamphetamine (MDMA) was synthesized in-house. All other chemicals were used as received.

2.2. Equipment

Ultraviolet/visible (UV/vis) absorption and fluorescence emission measurements were performed using a Varian Cary Eclipse spectrophotometer. Transmission electron microscopy (TEM) analysis were carried using a JEOL JEM-1200EX operated at 80 kV. Powder X-ray diffraction (PXRD) analysis was carried out using a Siemens D5000 diffractometer with Cu Kα radiation (λ = 1.54056 nm) and data were obtained in the range of 3–90° using a 0.1° 2θ step size and a 3 s count time per step with a 0.066° slit width. Dynamic light scattering (DLS) was carried out using a Zetasizer Nano ZS series (ZEN3600, Malvern). The Raman spectra were collected using an in-house built microprobe system equipped with a continuous wave laser sources emitting at 532 nm, the Oriel MS257 monochromator fitted with the Andor Newton EMCCD detector, TE cooled to − 70 °C. The backscattering configuration was used for the signal collection. The incident power on the samples was 63 mW. The spectra were recorded using a 40x objective (Plan Fluor, Nikon), a 0.3 s accumulation time with a total of 10 accumulations, a slit width of 100 mm and a 1200 lines/mm grating. Elemental analysis of the nanomaterials was carried out using a Philips 'Zetium' PW5400 X-ray fluorescence (XRF) used for sub ppm to percentage analysis of elements ranging from Be to Am, handled by a 35-position autosampler. Tube = PW2992/35 (zero-drift type); Anode = RhKα; Power = 2.4 kW; Collimator mask = 27 mm; Collimators = 150, 300 and 700 μm; Crystals = LiF200, Ge111, PE002, PX-1 and LiF220; Beam filters = brass 400 μm, brass 100 μm, Al 750 μm, Al 200 μm and Detectors = MCA flow, Sealed Xe and MCA Scint. Fourier transform-infrared (FT-IR) analysis was performed using an Agilent Cary 630 FT-IR spectrometer.

2.3. Preparation of precursors

Organic-phased HDA-capped Au nanoparticles (AuNPs) were synthesized via a ligand exchange reaction from hydrophilic citrate-AuNPs. To synthesize citrate-AuNPs, 1 mL 1% $HAuCl_4.3\ H_2O$ was mixed with ~79 mL H_2O and stirred at room temperature. Then, 20 mL aqueous solution containing 15.5 mL H_2O, 4 mL trisodium citrate, and 0.5 mL tannic acid was added into the Au precursor solution. The solution was stirred for ~15 min and heated up to a temperature of about 65 °C. Red-coloured solution of citrate-AuNPs were obtained. To obtain the organic-phased HDA-AuNPs, 2 g of HDA was dissolved in 20 mL of toluene and 50 mL of citrate-AuNPs was added. The solution was stirred for few seconds to aid separation of the aqueous-phased NPs from the organic-phased NPs. The HDA-AuNPs was carefully pipetted out of solution and stored in a sealed vial.

Zinc oleate was synthesized according to reported procedure for metal oleate synthesis but with some modification [50]. 13.6 g of zinc chloride was mixed with 18.25 g of sodium oleate in a mixture of 40 mL ethanol, 70 mL hexane and 30 mL MilliQ H_2O. The solution was heated up to ~85 °C and stirred for ~4 h (hr). The formed zinc oleate was purified using acetone, ethanol-chloroform and ethanol-acetone mixture.

The Se precursor was prepared by dissolving 0.14 g Se in 5 mL TOP while the sulphur precursor was prepared by mixing 0.16 g of sulphur with 0.9 g TOPO, 1 mL TOP, 10 mL octadecene and 5 mL oleic acid. Both the Se precursor and sulphur precursors were sonicated under heat for complete dissolution of the metal salt.

2.4. Synthesis of organic-phased AuZnFeSeS QDs

Organic-phased AuZnFeSeS QDs were synthesized using the standard organometallic hot-injection pyrolysis synthetic method for semiconductor QDs nanocrystals [51]. Briefly, 4 g $FeCl_3$, 5.6 g zinc oleate, 5 mL HDA-AuNPs, 2.4 g myristic acid, 0.6 g HDA, 5 mL oleylamine, 1.8 g TOPO, 2 mL TOP, 50 mL octadecene and 30 mL oleic acid were added into a three-necked flask and stirred under nitrogen atmosphere. The solution was heated up under vigorous stirring and after 40 min (min), the temperature reached ~210 °C. Thereafter, 3 mL of the Se precursor and all of the sulphur precursor solution were added into the AuZnFe precursor solution to aid the nucleation and growth of the AuZnFeSeS QDs. The organic-phased QDs was allowed to grow with time and the reaction was stopped after satisfactory fluorescence emission was obtained.

2.5. Preparation of SiO_2-AuZnFeSeS QDs

Surface encapsulation of the hydrophobic AuZnFeSeS QDs with SiO_2 was carried out according to literature procedure via a modified sol-gel approach [52]. The synthesized AuZnFeSeS QDs was mixed with chloroform and added into a solution containing 4 mL NH_3. OH in H_2O, 40 mL methanol, MilliQ H_2O, 10 mL TEOS and 8 mL APTES. The solution was stirred and heated up to approximately 70 °C for 45 min and the reaction was stopped after 1 hr. The SiO_2-AuZnFeSeS QDs were purified via ultracentrifugation using a mixture of acetone, acetone-Milli-Q H_2O, chloroform-acetone, and finally acetone.

2.6. Synthesis of SiO_2-AuZnFeSeS QDs@MIP nanocomposite

The synthesis of SiO_2-AuZnFeSeS QDs@MIP nanocomposite for levamisole fluorescence detection was carried out according to reported procedure but with some modifications [52,53]. In a beaker, 100 mg acrylamide, 2 mL EGDMA, 150 mg of purified SiO_2-AuZnFeSeS QDs, 100 mg levamisole template and 50 mg AIBN were mixed with 100 mL acetonitrile. The solution was stirred and heated up to approximately 73 °C for 2 hr 30 min. The obtained SiO_2-AuZnFeSeS QDs@MIP was then purified with acetone via ultracentrifugation to remove the levamisole template and thereafter dried in a fume hood. In order to validate the sensitivity of the SiO_2-AuZnFeSeS QDs@MIP towards levamisole detection, a non-imprinting SiO_2-AuZnFeSeS QDs@NIP was also prepared but without the levamisole template.

2.7. Fluorescence assay

A novel buffer containing a mixture of 2 g NaAc, 2 g KAc, 2 g Trizma® Ac, 5 g KSCN and 5 g borax in 250 mL of ultrapure MilliQ H_2O was prepared and the pH adjusted to 6. Thereafter, 200 μL of the purified AuZnFeSeS QDs@MIP nanocomposite (1 mg/mL) dissolved in the NaAc-KAc-Trizma® Ac-borax buffer solution pH 6 was mixed with 200 μL of levamisole (prepared in ultrapure MilliQ H_2O). The probe solution was measured ~15 s after adding levamisole (inclusive of the stirring time and start of the fluorescence scan) within the fluorescence wavelength range of 210–1100 nm at an excitation wavelength of 200 nm stirred.

3. Results and discussion

3.1. Fabrication of the AuZnFeSeS QDs@MIP nanocomposite

To fabricate the synthesis of the AuZnFeSeS QDs@MIP nanocomposite, AuZnFeSeS QDs was first synthesized in the organic phase and then surface-coated with SiO_2. Generally, metal chalcogenide of

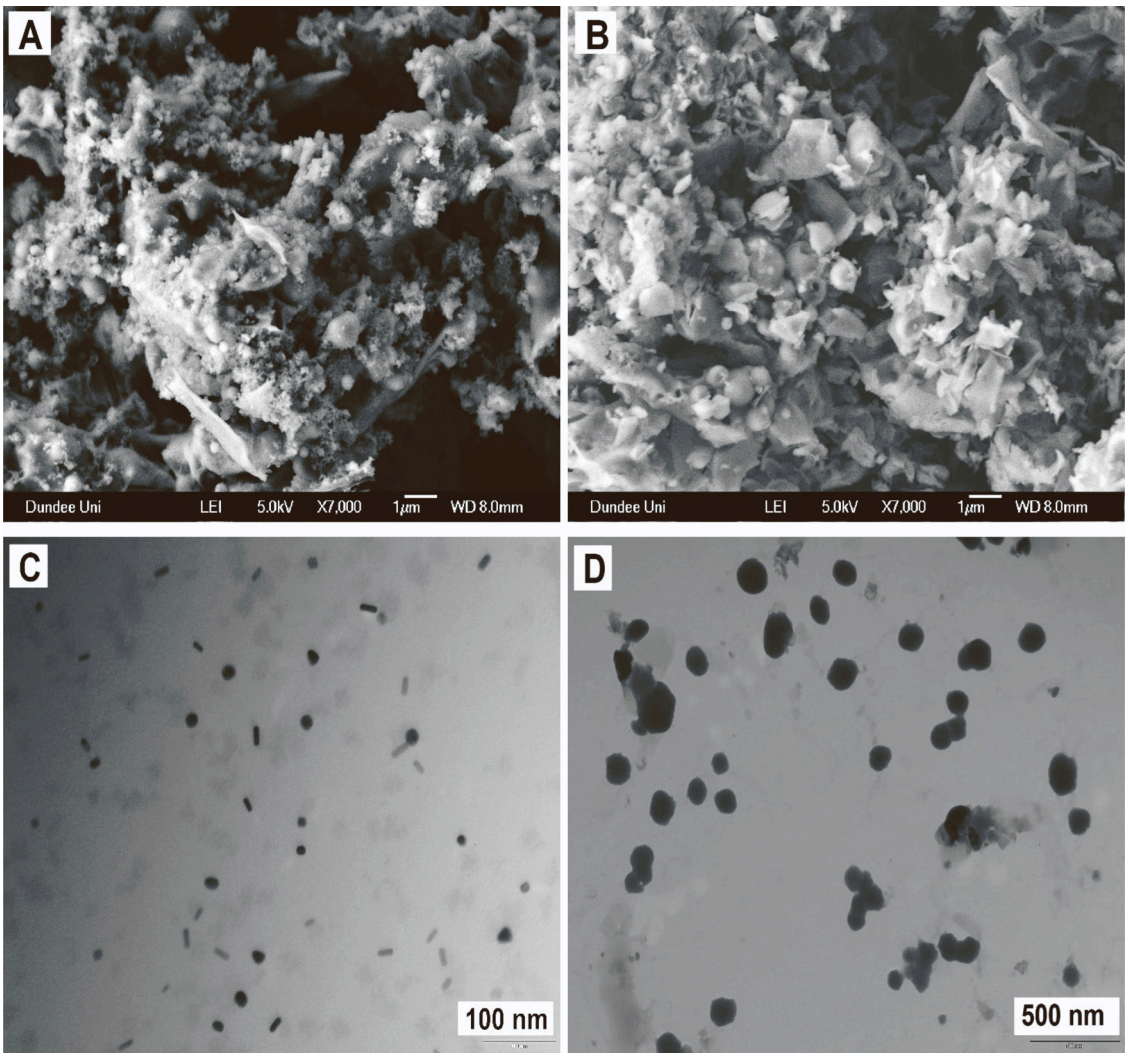

Fig. 1. SEM images and TEM images of the SiO_2-AuZnFeSeS QDs (A and C) and the AuZnFeSeS QDs@MIP nanocomposite (B and D).

groups II-V1 and III-V elements of the periodic Table have been widely used to develop QD-based nanostructures [54]. However, materials such as silicon, molybdenum, carbon and AuNPs, can also be used to alter the optical properties of the QDs [49]. Au was incorporated into the QDs nanostructure with the aim of obtaining a strong plasmon-exciton (electron and hole) interaction that could lead to the generate of new optical properties. Particularly, colloidal QDs are attractive nano-fluorophores for developing strong coupled systems with well-defined structures and nanometer precision due to their long exciton lifetime and large absorption cross section [55]. Hence, based on our previous study on the development of a polymeric-AuFeZnSe QDs [48], Au was embedded in the QDs nanostructure and additionally, S was introduced into the AuZnFeSe system to form a new NIR fluorescence-emitting AuZnFeSeS QDs.

Fig. S1 shows the UV/vis absorption spectra of citrate-AuNPs and that of HDA-AuNPs (prepared via a ligand exchange reaction of citrate-AuNPs). From the displayed data, HDA-AuNPs was characterized by a well pronounced surface plasmon resonance absorption peak at 531 nm which was not broadened or overly red-shifted in comparison to the absorption spectrum of citrate-AuNPs. This proves to show that HDA-AuNPs used in the synthesis of the QDs was not aggregated.

The synthesis of AuZnFeSeS QDs was carried out by reacting pre-mixed precursor solutions of HDA-AuNPs, $FeCl_3$, and zinc oleate in ODE together with organic surfactants such as HDA, oleylamine, TOPO, TOP and oleic acid. These organic surfactants functioned as capping agents to aid precise control of the QDs nucleation and growth. Both the $FeCl_3$ and zinc oleate precursors were found to decompose completely with the embedded surfactant solution above 200 °C within the timeframe of 40 min. Once complete dissolution was achieved, both TOPSe and TOPS precursors were added concurrently into the synthetic solution to aid the formation of the AuZnFeSeS alloyed QDs.

In the present study, we utilized excess amount of Fe and zinc oleate precursors which we believe allowed Se and S to react efficiently for the QDs nucleation and growth. Three reactions are generally expected to occur as illustrated in Eqs. (1–3):

$$\text{Au-FeZn } (O)_n + \text{TOPSe} \rightarrow (\text{Au-FeZnSe})(O)_m(T)_p \; k_1 \quad (1)$$

$$\text{Au-FeZn } (O)_n + \text{TOPS} \rightarrow (\text{Au-FeZnS})(O)_m(T)_p \; k_2 \quad (2)$$

$$X(\text{Au-FeZnSe})(O)_m(T)_p + Y(\text{Au-FeZnS})(O)_m(T)_p \rightarrow \text{Au-Fe}_w\text{Zn}_x\text{Se}_y\text{S}_z)(O)_m(T)_p \quad (3)$$

O represents the surfactants and/or solvent, T represents TOP, TOPO, TOPSe, TOPS, and k_1 and k_2 represents the rate constants of the synthetic reactions 1 and 2, respectively. Reaction 1 occurs between Au-ZnFe precursors and TOPSe to form Au-FeZnSe nuclei, and reaction 2 was formed between Au-ZnFe precursors and TOPS to form Au-FeZnS nuclei, representing reaction rate constant of k_1 and k_2, respectively. The crystal growth to form Au-$Fe_xZn_wSe_yS_z$ nanocrystals is represented by Reaction 3. It is imperative to emphasize that reactions 1–3 strongly depends on the nature of precursor type and their concentration,

solvent, and the reaction temperature used in this work. The solvents used in this work can be classified as non-coordinating, weakly coordinating, and coordinating solvents. ODE is classified as a non-coordinating solvent, whereas the other solvents are classified as having coordinating groups of varying donation power. TOPO (via the oxygen atom), TOPS (via the sulphur atom), oleic acid (via the oxygen atom), myristic acid (via the oxygen atom) and HDA (via amine) are metal-site-coordinating organic ligands, while TOP (via the phosphine atom) is a chalcogenide-metal-site coordinating ligand [56].

Fabrication of the AuZnFeSeS QDs@MIP nanocomposite involved the use of a free radical polymerization approach to overcoat the MIP as a shell layer around the AuZnFeSeS QDs core surface. Acrylamide was used as a functional monomer in solution with the SiO_2-AuZnFeSeS QDs to interact with levamisole template via a network of non-covalent hydrogen bonding interaction. EGDMA was used as the cross-linking reactive agent while AIBN was used as the polymerization initiator to drive the polymerization process to completion. Fig. S2 shows the molecular structure of the functional monomer, cross-linking agent, initiator, drug template, and the possible hydrogen bond formation between the monomer and the template.

3.2. Structural properties

Systematic manipulation of the shapes of inorganic nanocrystals remains a vital goal of modern materials chemistry research. The electro-optical properties of QDs are strongly dependent on the nanocrystal size and shape. SEM was used to probe the surface morphology of the SiO_2-AuZnFeSeS QDs and the AuZnFeSeS QDs@MIP nanocomposite. As shown in Fig. 1A and B, the morphology of the QDs and the QDs@MIP were each characterized by a porous and rough particle distribution with the particles stacked together in an irregular shape fashion. Fig. S3A and B shows the TEM images of HDA-capped AuNPs and the organic-phased AuZnFeSeS QDs. From the displayed data, HDA-capped AuNPs was characterized by a quasi-shaped spherical particle morphology while the morphology of the organic-phased AuZnFeSeS QDs revealed a well-defined spherical shaped particle distribution. As shown in Fig. 1C, the TEM image of the SiO_2-AuZnFeSeS QDs was characterized by a mixture of spherical and rod-shaped particles with the rod particles being more distributed than the spherical-shaped particles. The average particle size estimation was ~13 nm. The small size of the SiO_2-AuZnFeSeS QDs can be explained according to Smith and Nie proposed theory [57]. Smith and Nie proposed that the photostability, monodispersity and fluorescence quantum yield of polymer-capped QDs are strongly dependent on the optimal capping ratio. When the optimal capping ratio is approximately 1.5, it implies the QDs surface has been optimally coated with the appropriate number of polymers, yielding monodisperse, small-sized, highly photostable and high fluorescence quantum yield (> 50%) nanocrystals [57].

"Oriented attachment" is generally considered as the mechanism by which complex nanostructures are formed [58]. Via this mechanism, many interesting nanostructures can be formed because free surfaces are eliminated as a result of the nanocrystals being able to assemble together with optimum crystallographic alignment. Since the nanocrystal growth rate depends strongly on the monomer concentration, Oswald ripening occurs at low monomer concentration when small nanocrystal particles dissolve at the expense of larger-sized nanocrystals. Thus, such slow growth process favours spherical-shaped particle formation. Whereas, at high monomer concentration, the relative discrepancies between the growth conditions of different faces can trigger anisotropic shaped nanocrystal formation. In our work, we believe the growth rate of the QDs was superimposed between a slow and fast nucleation/growth process. On the other hand, we were able to control the growth condition of the different faces by precise variation in the ratio of the surfactants and capping agents and the use of HDA-AuNPs. It has also been reported that the inclusion of sodium oleate in seed-mediated synthesis of plasmonic nanoparticles can generate rod-shaped particles. In our work, sodium oleate was used in the synthesis of zinc oleate which we believe may have played a role in altering the shape dynamic of the QDs after the SiO_2 coating [59]. The rod-shaped SiO_2-AuZnFeSeS QDs aspect ratio was calculated as 2.0 according to Eq. (4) [60]:

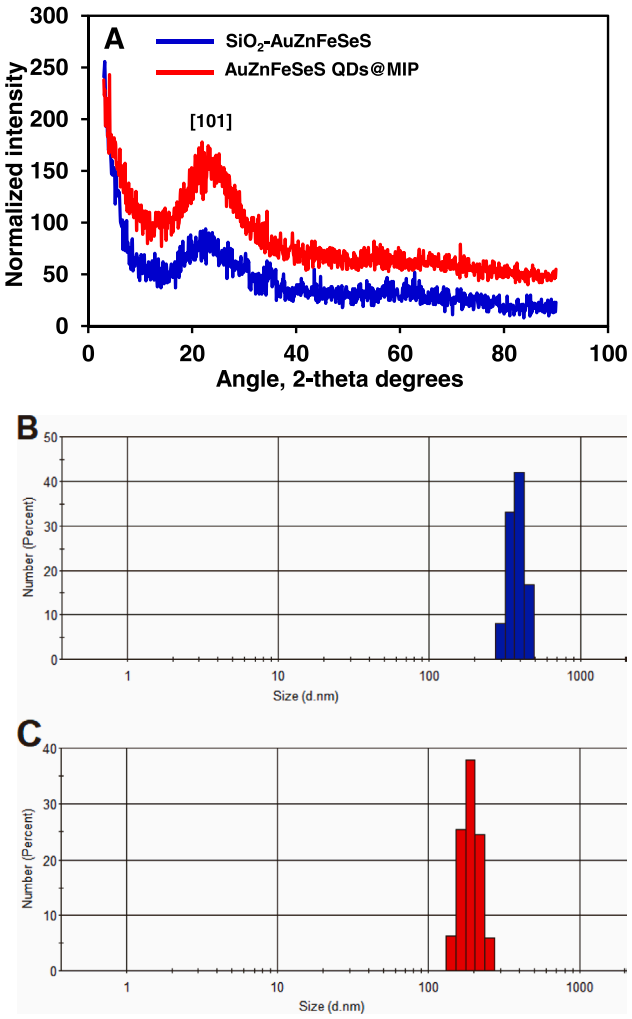

Fig. 2. (A) PXRD pattern of the SiO_2-AuZnFeSeS QDs and the AuZnFeSeS QDs@MIP nanocomposite. DLS histogram plots of the (B) SiO_2-AuZnFeSeS QDs and the (C) AuZnFeSeS QDs@MIP nanocomposite.

$$\lambda LSPR = 95R + 420 \quad (4)$$

Where $\lambda LSPR = 614$ nm.

As shown in Fig. 1D, the TEM image of the AuZnFeSeS QDs@MIP core/shell nanocomposite was characterized by a quasi-spherical shaped particle morphology with an average size of 130 nm. The absence of rod-shaped particles as observed for the QDs, suggest that the growth kinetics of the QDs was distorted as a result of the MIP process. The presence of several individual spherical particles across the TEM monograph confirms the monodispersed nature of the AuZnFeSeS QDs@MIP nanocomposite. Therefore, we ascertain that agglomeration of the particles was greatly suppressed during the MIP process.

Fig. 2A shows the PXRD pattern of the SiO_2-AuZnFeSeS QDs and the AuZnFeSeS QDs@MIP nanocomposite. From the data, it is clear that the diffraction pattern of both the QDs and the QDs@MIP nanocomposite are similar and dominated by a strong and broad diffraction peak at around plane 20°. It is evident that both diffraction patterns resemble that of amorphous silica [61] with no visible diffraction peak at > 30° due to the strong silica coating. Such diffraction feature has been reported previously for SiO_2-coated QDs [62].

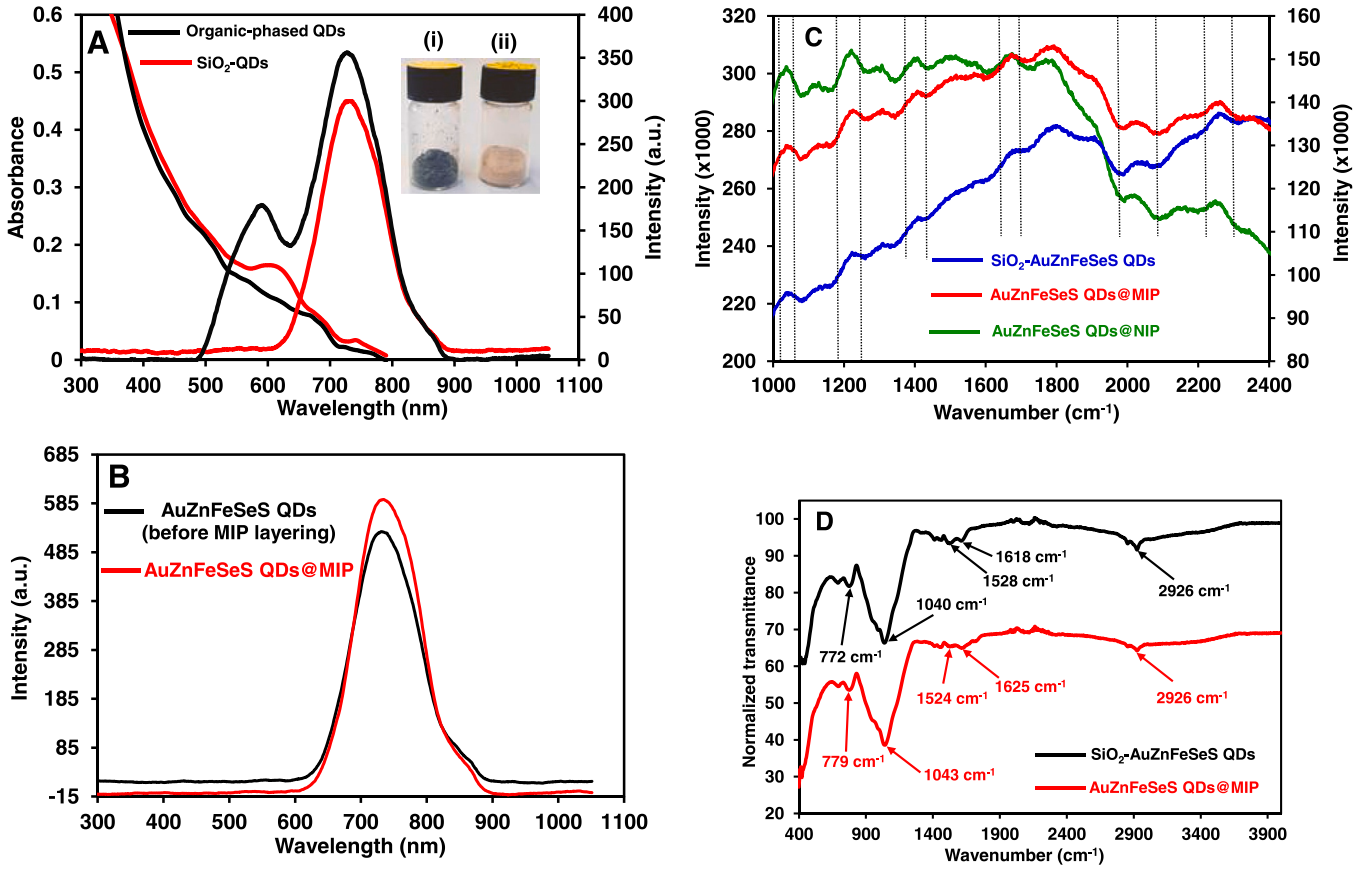

Fig. 3. (A) UV/vis absorption and fluorescence emission of the organic-phased AuZnFeSeS QDs and the SiO_2-AuZnFeSeS QDs. (B) Fluorescence emission spectra of the SiO_2-AuZnFeSeS QDs before and after layeing with the MIP shell. (C) Raman spectra of the SiO_2-AuZnFeSeS QDs, AuZnFeSeS QDs@MIP and the AuZnFeSeS QDs@NIP nanocomposites. (D) FT-IR spectra of the SiO_2-AuZnFeSeS QDs and the AuZnFeSeS QDs@MIP nanocomposite. Inset of Fig. 3A: Purified organic-phased AuZnFeSeS QDs and the SiO_2-AuZnFeSeS QDs in solid powdery form.

XRF was used to determine the elemental composition of the respective metal chalcogenides of the SiO_2-AuZnFeSeS QDs nanostructure. Due to the XRF instrumentation not been able to identify elements below sodium in the periodic table, only the elemental composition of Au, Zn, Fe, Se, S and Si were determined. Hence, hydrogen, carbon, oxygen and nitrogen moieties embedded within the SiO_2/MIP shell were not detected. The elemental composition values obtained for the SiO_2-AuZnFeSeS QDs are Au (0.03%), Zn (4.5%), Fe (33.2%), Se (0.14%), S (~0.1%), and Si (47.9%) while the values obtained for the AuZnFeSeS QDs@MIP are Au (~0.02%), Zn (~1.0%), Fe (22.8%), Se (0.06%), S (~1.7%), and Si (57.2%), respectively. From the results, all the metal components were each detected in the QDs and the QDs@MIP nanocomposite structure. However, in both the QDs and QDs@MIP nanocomposite, the %composition of Fe and Si were high while those of Au, Se, and S were very low. Generally, comparing the individual values of each metal in the QDs and the QDs@MIP nanocomposite, only the %composition of Si increased in the QDs@MIP nanocomposite relative to the QDs. Based on the observed results, the % composition of each metal obtained in the QDs@MIP nanocomposite may be a reflection of the MIP shelling process.

3.3. Optical properties

DLS was used to probe the polydispersity of the colloidal SiO_2-AuZnFeSeS QDs and the AuZnFeSeS QDs@MIP nanocomposite in solution. Fig. 2B and C shows the hydrodynamic histogram size plots of the SiO_2-AuZnFeSeS QDs and the AuZnFeSeS QDs@MIP nanocomposite. The size value obtained were ~381 nm for the SiO_2-AuZnFeSeS QDs and ~192 nm for the AuZnFeSeS QDs@MIP nanocomposite. Generally, hydrodynamic size value > 100 indicate that the colloidal NP is polydisperse in solution. However, bulky surface capping moieties such as SiO_2 can induce high polydispersity index for nanomaterials in solution as we have observed in this work. Interestingly, we observed a reduction in the hydrodynamic size of the AuZnFeSeS QDs@MIP nanocomposite in comparison to the SiO_2-AuZnFeSeS QDs. This indicates that the MIP shell effectively passivated the surface of the QDs.

UV/vis absorption and fluorescence emission spectra of the organic-phased AuZnFeSeS QDs and the SiO_2-AuZnFeSeS QDs are shown in Fig. 3A. For the organic-phased AuZnFeSeS QDs, the UV/vis absorption spectrum was characterized by an excitonic absorption peak at around 646 nm while for the SiO_2-AuZnFeSeS QDs, the UV/vis absorption spectrum was characterized by an excitonic absorption peak maximum at ~610 nm. The blue shift in the excitonic absorption peak of the SiO_2-AuZnFeSeS QDs relative to the organic-phased AuZnFeSeS QDs may be due to the SiO_2 coating. For the organic-phased AuZnFeSeS QDs, the fluorescence emission spectrum was projected at a wavelength maximum of 728 nm while for the SiO_2-AuZnFeSeS QDs, the fluorescence emission was projected at ~732 nm. It was clearly evident that the respective precursor materials used in the QDs synthesis triggered the near-infrared fluorescence emission properties of the QDs. Surprisingly, the fluorescence emission of the QDs was not overly broad and no observable peak tailing at lower energy associated with deep trap state was seen. The inset of Fig. 3A shows the purified powdery particle form of the organic-phased AuZnFeSeS QDs and the SiO_2-AuZnFeSeS QDs. From the display of the particles, it was evident that SiO_2 coating on the QDs surface changed the particle colour from greyish black to light

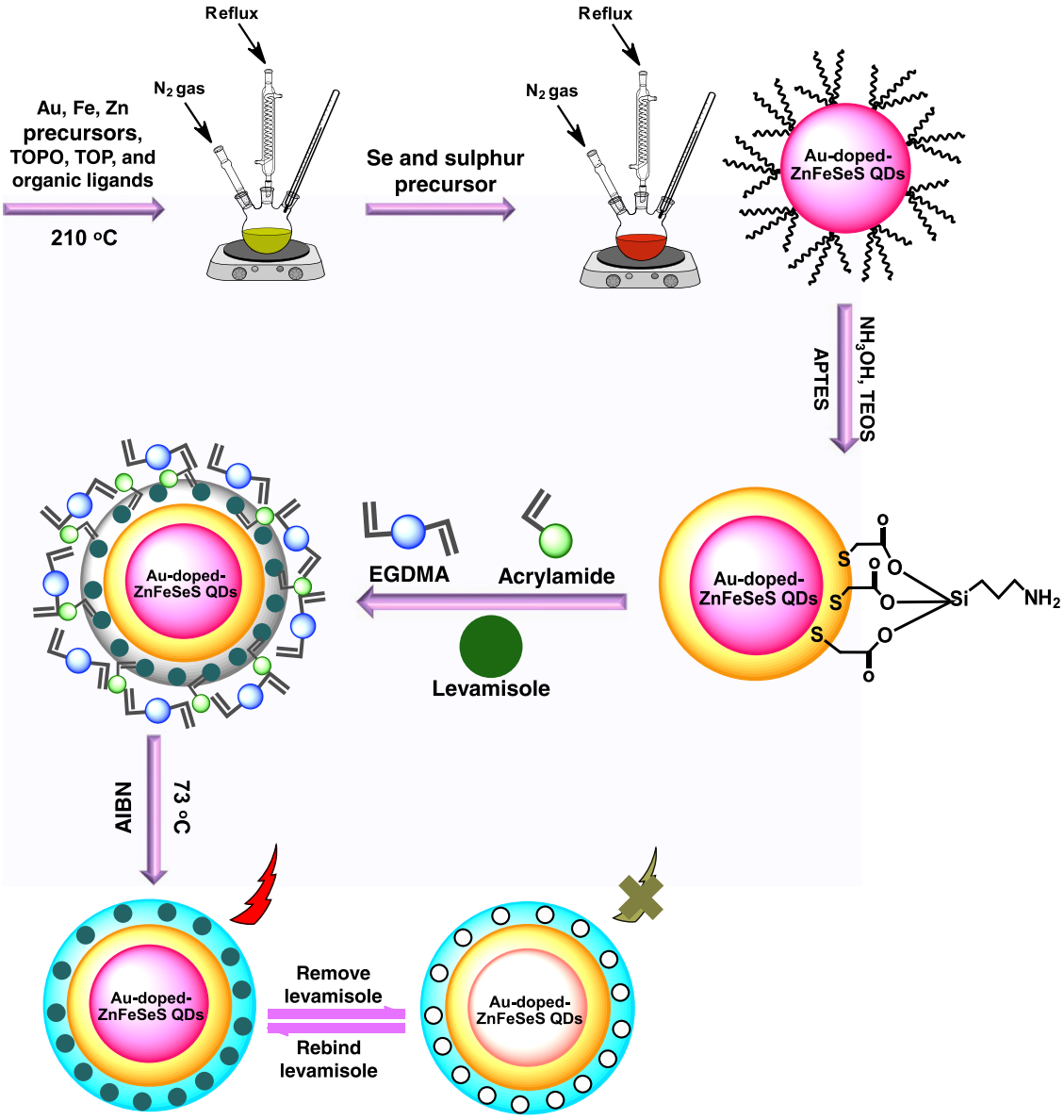

Scheme 1. Schematic representation of the SiO_2-AuZnFeSeS QDs@MIP nanocomposite synthetic preparation and detection mechanism for levamisole recognition.

brown.

The fluorescence quantum yield of the QDs which is the ratio of photon emitted to photon absorbed was measured according to Eq. (5) to assess the photophysical properties of the QDs as it relates to its surface passivating efficiency and sensitivity:

$$\Phi_F^{QDs} = \Phi_F^{RHO}\frac{F_{QDs}.OD_{RHO(\lambda exc)}.n^2_{water}}{F_{RHO}.OD_{QDs(\lambda ex)}.n^2_{ethanol}} \quad (5)$$

Φ_F^{QDs} represents the fluorescence quantum yield of the QDs, Φ_F^{RHO} represents the fluorescence quantum yield of rhodamine 6 G ($\Phi = 0.95$) which was used as the reference standard [63], F_{QDs} and F_{RHO} represents the integrated sum of the fluorescence intensity of the QDs and rhodamine standard, $OD_{RHO(\lambda exc)}$ and $OD_{QDs(\lambda exc)}$ represents the absorbances of the rhodamine standard and QDs, while n^2_{water} and $n^2_{ethanol}$ represents the squares of the refractive index of the QDs and rhodamine solvents, respectively. The estimated fluorescence quantum yield of the SiO_2-AuZnFeSeS QDs was 66%. The value obtained was quite high for QDs emitting in the near-infrared region. The value proves to show that surface defect states in the QDs was suppressed to greater degree.

As shown in Fig. 3B, the fluorescence of the SiO_2-AuZnFeSeS QDs was enhanced after layering with the MIP shell. No significant peak broadening or red shifting of the AuZnFeSeS QDs@MIP fluorescence was observed in comparison to the fluorescence of the QDs (before MIP layering). This proves to show that the fluorescence of the AuZnFeSeS QDs@MIP nanocomposite was stable. The lack of peak tailing associated with deep trap state also confirms the fluorescence stability of the AuZnFeSeS QDs@MIP nanocomposite. Therefore, we can conclude that SiO_2 passivation of the AuZnFeSeS QDs surface contributed to the QDs compactness and photostability whilst also aiding robust MIP shell layering.

Raman analysis was used to probe the vibrational characteristics and surface properties of the SiO_2-AuZnFeSeS QDs, AuZnFeSeS QDs@MIP and the AuZnFeSeS QDs@NIP nanocomposites. As shown in Fig. 3C, the Raman scattering spectra of the SiO_2-AuZnFeSeS QDs, AuZnFeSeS QDs@MIP and the AuZnFeSeS QDs@NIP nanocomposites were projected at different intensities with all spectra almost having almost the same longitudinal optical phonons but with varying degree of peak shift and broadening. The difference in intensities gives strong credence to the variation in surface properties of the respective nanomaterials. For the SiO_2-AuZnFeSeS QDs, the vibrational bands from 1200 to 1650 cm^{-1}

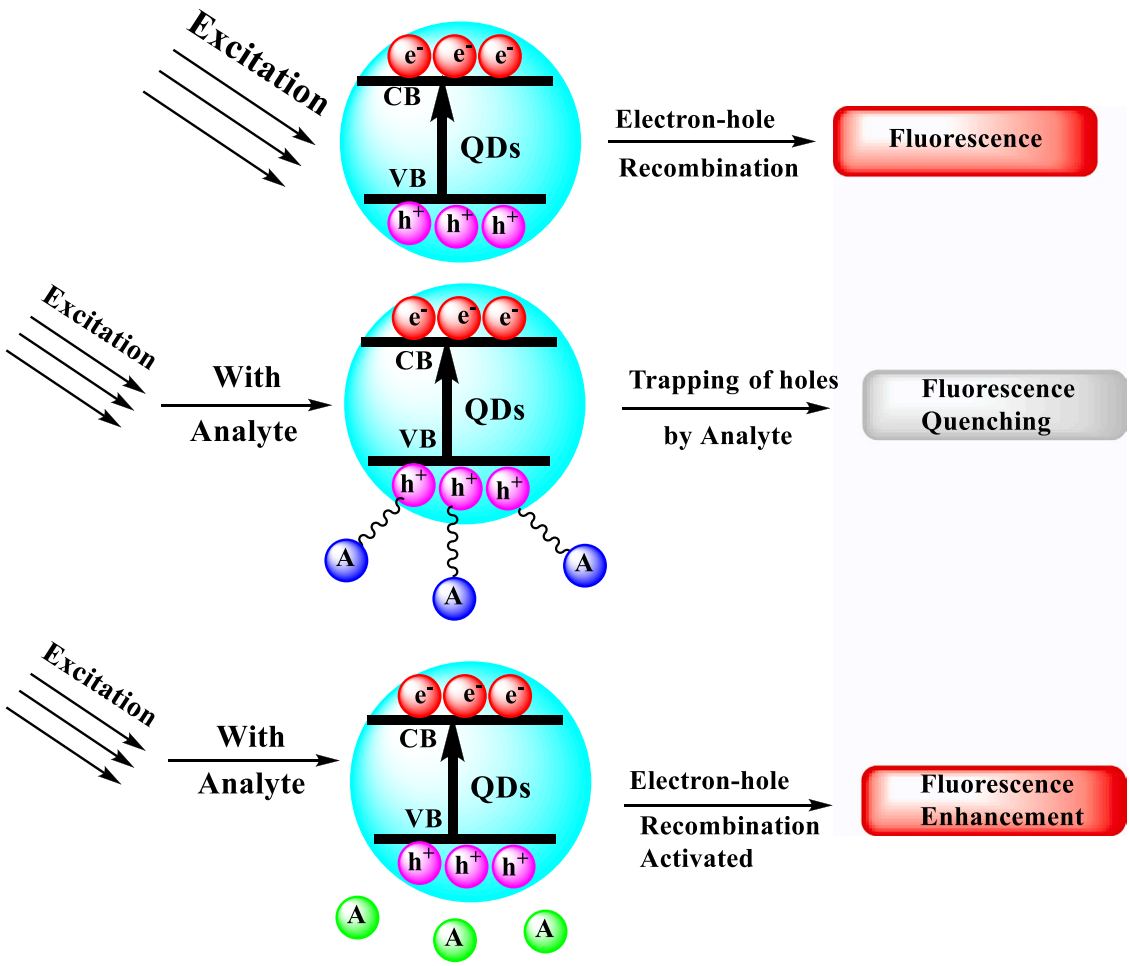

Scheme 2. Schematic representation of band structure of QDs showing the excited state fluorescence processes. VB = Valence band and CB = conduction band. Analyte (A) is used to represent the surface interacting component.

were more broadened than for the other tested hybrid nanocomposites. This may provide strong evidence of the lack of polymerization on the QDs surface. One notable observation was that the Raman peaks of the AuZnFeSeS QDs@NIP nanocomposites at 1050, 1250 and 1400 cm^{-1} were narrower than the peaks for the AuZnFeSeS QDs@MIP nanocomposite. This observable feature may be used as the basis to differentiate the imprinted levamisole template from the non-imprinted template.

The FT-IR spectra of the SiO_2-AuZnFeSeS QDs and the AuZnFeSeS QDs@MIP nanocomposite are shown in Fig. 3D. From the obtained results, the peaks at 772 cm^{-1} and 1040 cm^{-1} for the QDs and 779 cm^{-1} and 1043 cm^{-1} for the QDs@MIP, corresponds to the Si-O and Si-O-Si stretching vibrations respectively. This proves to confirm the presence of the SiO_2 coating on the QDs surface and its embedment within the MIP shell layer. The peak at 1528 cm^{-1} for the QDs and 1524 cm^{-1} for the QDs@MIP, can be assigned to the C = C bending vibration. The peaks at 1618 cm^{-1} and 2926 cm^{-1} for the QDs and 1625 cm^{-1} and 2926 cm^{-1} for the QDs@MIP, can be assigned to the CO-NH and C-H stretching vibrations respectively. Generally, the expected functional moieties on the QDs and the QDs@MIP surface were all identified in the projected FT-IR spectra. The peak shift observed in some of the functional groups on the QDs@MIP surface relative to the unbound QDs, may be due to the effects of the MIP shell layering.

3.4. Mechanism of the detection

The mechanism of the AuZnFeSeS QDs@MIP nanocomposite for levamisole detection as shown in Scheme 1 follows the general principle of template imprinting, template removal and template re-binding. As shown in Scheme 1, AuZnFeSeS QDs were synthesized in the organic phase via the organometallic hot injection pyrolysis of metal precursors. To coat the QDs surface with SiO_2, APTES was used as the functional monomer, TEOS was used as the cross-linker and NH_3. OH in H_2O was used as the catalyst. SiO_2 coating on the QDs surface served as a rigid passivating layer to render the QDs compact, stable, and biocompatible. The amino groups of APTES can interact non-covalently via hydrogen bond formation with the functional moiety of the acrylamide monomer. Acrylamide monomer can also interact non-covalently with the template levamisole while the presence of EGDMA and AIBN allows the polymerization process to reach completion with the embedded levamisole template. The levamisole template was then removed from the MIP layer in which the removal process led to the formation of cavities specific to the size and shape of levamisole. Detection of levamisole was achieved via a rebinding process on the MIP layer while the bound QDs transduces the signal of the rebinding process in the form of changes in the fluorescence intensity. Generally, MIP shell coating on the QDs surface led to fluorescence enhancement of the QDs with the enhancement process thought to emanate from the radiative exciton (electron and hole) recombination process of the QDs. However, the rebinding process of levamisole on the MIP layer led to quenching of the bound QDs fluorescence and such process can be thought to emanate from the non-radiative exciton recombination process of the QDs.

Scheme 2 shows the descriptive QDs excited state processes. When the QDs is excited, an electron-hole pair is formed where electron from

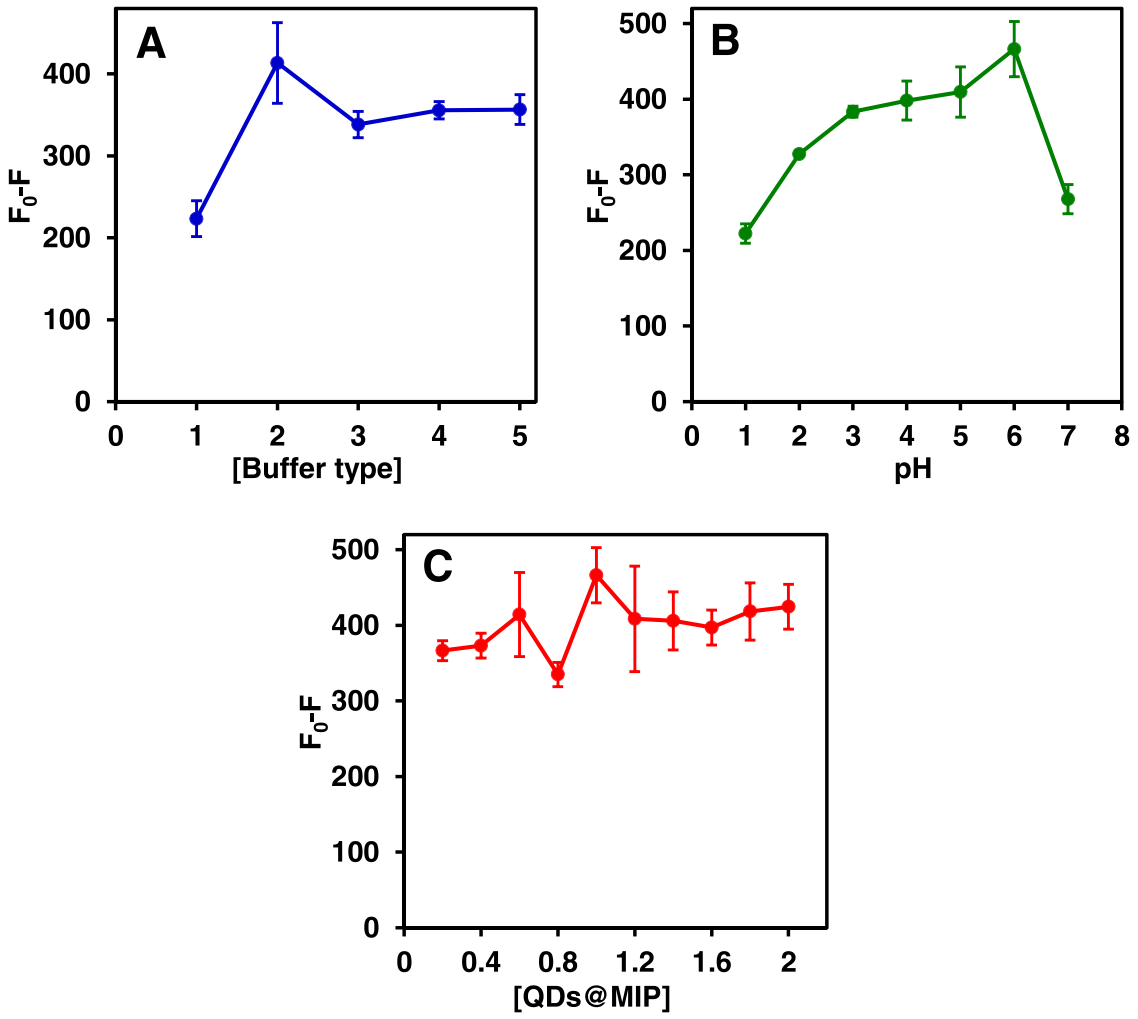

Fig. 4. Effect of buffer type (A), pH (B) and the AuZnFeSeS QDs@MIP nanocomposite concentration (C) on the fluorescence intensity of the AuZnFeSeS QDs@MIP nanocomposite for levamisole detection. Buffer 1 = NaAc-KAc-MES-KSCN-borax; buffer 2 = NaAc-KAc-Trisma Ac-KSCN-borax; buffer 3 = NH_4Ac-Trisma Ac-MES-KSCN-borax; buffer 4 = NH_4Ac-NaAc-KCl-KSCN-borax, and buffer 5 = NH_4Ac-KAc-Trisma Ac-KSCN-borax. [Levamisole] = 100 μM in Milli-Q H_2O. F_0 (Control) = AuZnFeSeS QDs@MIP nanocomposite (1 mg/mL) dissolved in the NaAc-KAc-Trizma® Ac-borax buffer solution pH 6. F = Fluorescence intensity signal for levamisole detection.

the valence band is promoted to the conduction band via energy absorption. This process then leaves behind a positive charged hole of opposite electric charge in the valence band. The promoted electron is generally bound to the hole by coulomb force. Recombination of the electron-hole pair occurs when the QDs is excited to generate emission light of certain wavelength which corresponds to the QDs bandgap energy. When the QDs fluorescence is quenched, the electron-hole recombination process is inhibited because the hole becomes trapped by surface interacting components. This process leads to the generation of non-radiative emission light. Conversely, when the QDs fluorescence is enhanced, the electron-hole recombination process is activated leading to the generation of radiative emission light [64].

3.5. Optimization of the fluorescence assay

Prior to optimizing the fluorescence assay for levamisole, we studied the effect of the MIP shell layering on the SiO_2-AuZnFeSeS QDs fluorescence in different buffer systems and at different pH with the discussion and data provided in the Supplementary Information section (Fig. S4A-C). In order to study the effect of buffer type on the fluorescence detection of levamisole using the AuZnFeSeS QDs@MIP nanocomposite, five novel buffer solutions composed of NaAc-KAc-MES-KSCN-borax (buffer 1), NaAc-KAc-Trisma Ac-KSCN-borax (buffer 2), NH_4Ac-Trisma Ac-MES-KSCN-borax (buffer 3), NH_4Ac-NaAc-KCl-KSCN-borax (buffer 4) and NH_4Ac-KAc-Trisma Ac-KSCN-borax (buffer 5), were prepared. Both the SiO_2-AuZnFeSeS QDs and the AuZnFeSeS QDs@MIP nanocomposite were dissolved in each buffer system while levamisole was prepared in ultrapure Milli-Q water. As shown in Fig. 4A, the generated fluorescence signal for levamisole was specific for each tested buffer system. From our result, the efficiency of the fluorescence signal for levamisole detection followed the order: buffer 2 > buffer 5 > buffer 4 > buffer 3 > buffer 1. Hence, buffer 2 was chosen as the choice buffer for the fluorescence assay.

The effect of pH using the choice buffer 2 was studied for levamisole detection using the AuZnFeSeS QDs@MIP nanocomposite. As shown in Fig. 4B, the obtained fluorescence signal increased steadily as the pH increased and peaked at pH 6, then decreased sharply at pH 7. It is important to note that the measured fluorescence intensity signal was strongly dependent on the ionic strength of the QDs sample. This is due to the complex relationship between proton activity and the pH sensitive QDs concentration. Hence, the sudden decrease in the fluorescence intensity signal of the AuZnFeSeS QDs@MIP probe at pH 7 can be explained to this effect. Based on our result, pH 6 was chosen as the choice pH for levamisole detection. Fig. 4C shows the effect of the AuZnFeSeS QDs@MIP nanocomposite concentration on the fluorescence response of levamisole studied from 0.2 to 2 mg/mL. From the observed

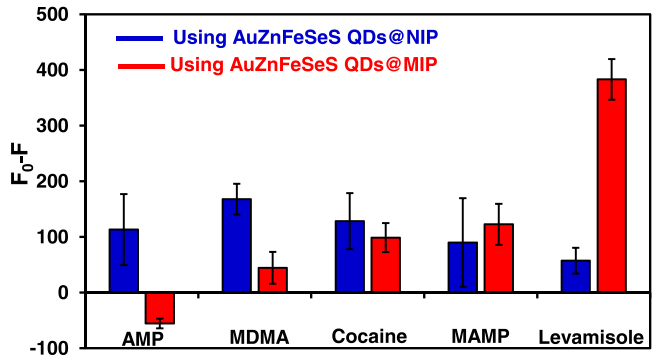

Fig. 5. (A) Fluorescence intensity signal of the AuZnFeSeS QDs@MIP nanocomposite for levamisole detection in comparison to other tested drugs. The fluorescence intensity signal of the AuZnFeSeS QDs@NIP for levamisole and other tested drugs is also shown for comparison. [Drugs] = 100 μM in Milli-Q H_2O. F_0 (Control) = AuZnFeSeS QDs@MIP or AuZnFeSeS QDs@NIP nanocomposite (1 mg/mL) dissolved in the NaAc-KAc-Trizma® Ac-borax buffer solution pH 6. F = Fluorescence intensity signal for levamisole detection.

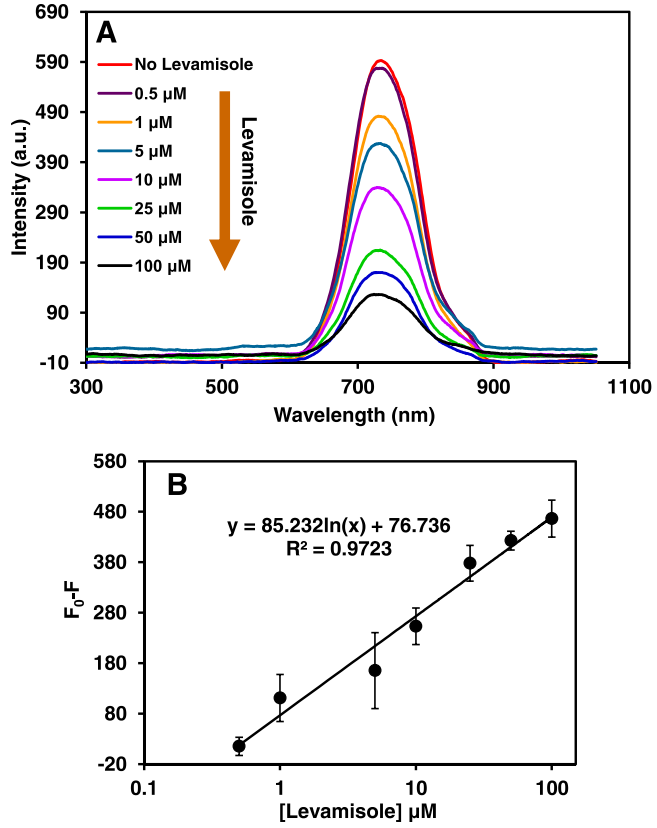

Fig. 6. (A) Fluorescence emission spectra of the AuZnFeSeS QDs@MIP nanocomposite for levamisole quantitative detection and (B) the corresponding calibration signal plot. Inset: linear calibration plot for levamisole detection. F_0 (Control) = AuZnFeSeS QDs@MIP nanocomposite (1 mg/mL) dissolved in the NaAc-KAc-Trizma® Ac-borax buffer solution pH 6. F = Fluorescence intensity signal for levamisole detection.

data, the generated fluorescence signal for levamisole increased from 0.2 to 0.6 mg/mL, then decreased sharply at 0.8 mg/mL and reached optimum fluorescence signal at 1 mg/mL. At 1.2 mg/mL, the fluorescence intensity signal decreased sharply relative to the signal at 1.0 mg/mL whilst the observed signal trend up until 2.0 mg/mL exhibited near equilibrium in the generated data. Hence, 1 mg/mL AuZnFeSeS QDs@MIP concentration was chosen as the choice concentration for levamisole detection.

3.6. Selectivity of the fluorescence assay

The selectivity of the AuZnFeSeS QDs@MIP and AuZnFeSeS QDs@NIP nanocomposites towards levamisole was investigated. Cocaine which is usually laced with levamisole and other common illicit drugs such as MDMA, AMP and MAMP were used as interferents to probe the selectivity of the developed fluorescence assay. As shown in Fig. 5, using the AuZnFeSeS QDs@MIP probe, the fluorescence signal obtained for levamisole was far superior to the fluorescence response obtained for the tested interferent drugs. More importantly, the fluorescence signal for levamisole was at least 3-fold higher than the fluorescence signal for MAMP. Conversely, using the AuZnFeSeS QDs@NIP nanocomposite, no selectivity towards levamisole was achieved. This demonstrates that the AuZnFeSeS QDs@NIP did not exhibit the required affinity for levamisole recognition. Based on our result, it is appropriate to conclude that the developed AuZnFeSeS QDs@MIP nanocomposite possesses high affinity for levamisole due to the drug being able to selectively rebind into the created cavities of the MIP shell.

3.7. Quantitative levamisole detection

Quantitative detection of levamisole was carried out to validate the efficacy of the AuZnFeSeS QDs@MIP nanocomposite to detect different concentrations of the drug. The concentration of levamisole was detected in the range of 0.5 – 100 μM as shown in Fig. 6A and B. In Fig. 6A, increasing concentration of detected levamisole was directly reflected in the simultaneous and steady symmetric decrease in the fluorescence emission spectra of the AuZnFeSeS QDs@MIP nanocomposite. Most importantly, the fluorescence spectra of the AuZnFeSeS QDs@MIP nanocomposite upon levamisole quantitative detection did not result in any significant spectral shift or broadening. This demonstrated the unique fluorescence emission stability of the AuZnFeSeS QDs@MIP nanocomposite. The corresponding fluorescence calibration signal plot shown in Fig. 6B revealed that levamisole detection followed a linear regression pattern. The limit of detection (LOD) was determined by multiplying the standard deviation of blank measurement (n = 10; 1.348) by three and dividing by the obtained calibration slope value (slope = 85.232). The obtained LOD for levamisole detection was 47.4 nM.

Furthermore, the efficacy of the AuZnFeSeS QDs@NIP nanocomposite to quantitatively detect levamisole was investigated. As shown in Fig. S5, levamisole could not be detected quantitatively using the AuZnFeSeS QDs@NIP nanocomposite as the response obtained lacked a symmetric signal intensity trend, clearly indicating that the AuZnFeSeS QDs@NIP nanocomposite lacked the affinity to rebind levamisole. Thus, the unsymmetric intensity signal generated showed clearly that the AuZnFeSeS QDs@NIP nanocomposite did not function as an affinity-based fluorescence probe for levamisole.

3.8. Detection in mixed drug sample

Detection of levamisole in mixed drug sample containing cocaine was carried out to validate the efficacy of the AuZnFeSeS QDs@MIP nanocomposite to detect levamisole within such a sample. Since

Table 1
Analytical parameters of the AuZnFeSeS QDs@MIP nanocomposite probe for levamisole detection in mixed drug sample containing cocaine.

Cocaine, μM	Levamisole added, μM	Found (μM)	Recovery (%)	RSD (%, n = 3)
100	100	92.6	92.6	4.7
	50	50.5	101.1	8.3
	10	~10.1	100.9	1.8

Table 2
Comparison of the analytical parameters of the AuZnFeSeS QDs@MIP nanocomposite sensor for levamisole detection with other published probes.

Probe	Method	Concentration range	Applicable detection Matrix	LOD (nM)	Ref.
Glycosylated metalloporphyrin	Fluorescence	0.35–13 μM	Buffer	350	[65]
MIP	Potentiometry	100 mM – 13 μM	H_2O	1000	[12]
High-performance liquid chromatography (HPLC)	Chromatographic separation	0.01–10 μg/mL	Plasma	87	[66]
HPLC	Chromatographic separation	1–20 μg/mL	Plasma and ruminal fluid	83.1–207.7	[67]
Reverse phase -HPLC	Chromatographic separation	15–45 μg/mL	Methanol	8640	[68]
AuZnFeSeS QDs@MIP nanocomposite	Fluorescence	0. 5–100 μM	H_2O and mixed drug	47.4	This work

levamisole is commonly mixed with cocaine, a series of levamisole-cocaine samples were prepared by mixing different concentrations of levamisole with a fixed concentration of cocaine. As shown in Table 1, different concentrations of levamisole were successfully detected in the prepared mixtures using the AuZnFeSeS QDs@MIP nanocomposite with satisfactory analytical recoveries. The obtained result clearly demonstrates the efficacy of the AuZnFeSeS QDs@MIP nanocomposite to sensitively detect different concentrations of levamisole within the mixed drug sample.

Table 2 shows the comparison of the analytical parameters of the AuZnFeSeS QDs@MIP fluorescence probe with other published techniques. From the comparative data, the LOD obtained for levamisole recognition was lower than the published values obtained from other techniques. Also, none of the other techniques demonstrated the efficacy of detecting levamisole in an adulterated cocaine sample which we have successfully demonstrated in this work.

4. Conclusions

In this work, we have successfully fabricated the development of a novel AuZnFeSeS QDs@MIP nanocomposite fluorescent probe for levamisole detection in water and in mixed drug sample. SiO_2- AuZnFeSeS QDs was synthesized via the hot-injection organometallic pyrolysis of metal precursors and was surface-coated with SiO_2 to generate a compact, stable and biocompatible QDs system. Using a free radical polymerization synthetic approach, a core/shell AuZnFeSeS QDs@MIP nanocomposite fluorescent probe was developed for levamisole. We successfully proved the strong affinity of the MIP-levamisole binding interaction based on the symmetric quantitative fluorescence signal obtained using the AuZnFeSeS QDs@MIP nanocomposite. The AuZnFeSeS QDs@MIP nanocomposite probe was highly selective for levamisole with the fluorescent signal being at least 3-fold higher than the fluorescence response obtained from other tested drugs. Quantitative detection of levamisole was accomplished with high sensitivity over other published techniques. Finally, we successfully detected levamisole in mixed drug sample containing cocaine with satisfactory recoveries.

CRediT authorship contribution statement

Oluwasesan Adegoke: Conceptualization, Investigation, Methodology, Writing – original draft and Writing – review & editing. **Svetlana Zolotovskaya**: Research fund acquisition, Raman analysis and Writing – review & editing. **Amin Abdolvand**: Research fund acquisition, Raman analysis and Writing – review & editing. **Niamh Nic Daeid:** Research fund acquisition and Writing – reviewing and editing.

Declaration of Competing Interest

The authors declare that they have no known competing financial interests or personal relationships that could have appeared to influence the work reported in this paper.

Acknowledgements

Authors gratefully acknowledge the financial support from Leverhulme Trust for funding this work. Authors would also like to acknowledge the support received from Engineering and Physical Sciences Research Council (EPSRC) through EP/P008135/2 and EP/S017445/1. OA sincerely appreciates the support received from the School of Science and Engineering, University of Dundee.

Appendix A. Supporting information

Supplementary data associated with this article can be found in the online version at doi:10.1016/j.colsurfa.2022.129013.

References

[1] C. Auffenberg, L.J. Rosenthal, N. Dresner, Levamisole: a common cocaine adulterant with life-threatening side effects, Psychosomatics 54 (2013) 590–593.
[2] N.Y. Zhu, D.F. Legatt, A.R. Turner, Agranulocytosis after consumption of cocaine adulterated with levamisole, Ann. Intern. Med. 150 (2009) 287–289.
[3] A. Chang, J. Osterloh, J. Thomas, Levamisole: a dangerous new cocaine adulterant, Clin. Pharmacol. Ther. 88 (2010) 408–411.
[4] K. Ullrich, R. Koval, E. Koval, S. Bapoje, J.M. Hirsh, Five consecutive cases of a cutaneous vasculopathy in users of levamisole-adulterated cocaine, J. Clin. Rheuma 17 (2011) 193–196.
[5] C.S. Tallarida, E. Egan, G.D. Alejo, R. Raffa, R.J. Tallarida, S.M. Rawls, Neuropharmacology 79 (2014) 590–595.
[6] H. De Ruyck, R. Van Renterghem, H. De Ridder, D. De Brabander, Determination of anthelmintic residues in milk by high performance liquid chromatography, Food Control 11 (2000) 165–173.
[7] S.J. Stout, A.R. DaCunha, R.E. Tondreau, J.E. Boyd, Confirmation of levamisole residues in cattle and swine livers by capillary gas chromatography-electron impact mass spectrometry, J. Assoc. Anal. Chem. 71 (6) (1988) 1150–1153.
[8] A. Cannavan, W.J. Blanchflower, D.G. Kennedy, Determination of levamisole in animal tissues using liquid chromatography–thermospray mass spectrometry, Analyst 120 (1995) 331–333.
[9] F.J. Schenck, L.V. Podhorniak, R. Wagner, A highly sensitive gas chromatographic determination of levamisole in milk, Food Addit. Contam. 15 (4) (1998) 411–414.
[10] S.R.H. Crooks, B. McCarney, I.M. Traynor, X.S. Thompson, S. Floyd, C.T. Elliott, Detection of levamisole residues in bovine liver and milk by immunobiosensor, Anal. Chim. Acta 483 (2013) 181–186.
[11] J.J. Silverlight, R. Jackman, Enzyme immunoassay for the detection of levamisole in meat and milk, Analyst 119 (1994) 2705–2706.
[12] S. Sadeghi, F. Fathi, J. Abbasifar, Potentiometric sensing of levamisole hydrochloride based on molecularly imprinted polymer, Sens. Actuators B 122 (2007) 158–164.
[13] A. Poma, A. Guerreiro, M.J. Whitcombe, E.V. Piletska, A.P.F. Turner, S.A. Piletsky, Solid-phase synthesis of molecularly imprinted polymer nanoparticles with a reusable template–"plastic antibodies", Adv. Funct. Mater. 23 (2013) 2821–2827.
[14] K. Haupt, Molecularly imprinted polymers: the next generation, Anal. Chem. 75 (2003) 376A–383A.
[15] K. Haupt, K. Mosbach, Molecularly imprinted polymers and their use in biomimetic sensors, Chem. Rev. 100 (2000) 2495–2504.
[16] G. Wulff, A. Sarhan, Use of polymers with enzyme-analogous structures for the resolution of racemates, Angew. Chem., Int. Ed. 11 (1972) 341.
[17] J.J. BelBruno, Molecularly imprinted polymers, Chem. Rev. 119 (2019) 94–119.
[18] L. Ye, P.A.G. Cormack, K. Mosbach, Molecularly imprinted monodisperse microspheres for competitive radioassay, Anal. Commun. 36 (1999) 35–38.
[19] D. Vaihinger, K. Landfester, I. Kräuter, H. Brunner, G.E.M. Tovar, Molecularly imprinted polymer nanospheres as synthetic affinity receptors obtained by miniemulsion polymerisation, Macromol. Chem. Phys. 203 (2002) 1965–1973.
[20] P. Çakir, A. Cutivet, M. Resmini, B. Tse Sum Bui, K. Haupt, Protein-size molecularly imprinted polymer nanogels as synthetic antibodies, by localized polymerization with multi-initiators, Adv. Mater. 25 (2013) 1048–1051.
[21] Y. Zhao, C. Simon, M.D. Attieh, K. Haupt, A.Falcimaigne-Cordin, Reduction-responsive molecularly imprinted nanogels for drug delivery applications, Rsv. Adv. 10 (2020) 5978–5987.
[22] E. Yilmaz, K. Haupt, K. Mosbach, The use of immobilized templates- a new approach in molecular imprinting, Angew. Chem., Int. Ed. 39 (2000) 2115–2118.
[23] S. Ambrosini, S. Beyazit, K. Haupt, B. Tse Sum Bui, Solid-phase synthesis of molecularly imprinted nanoparticles for protein recognition, Chem. Commun. 49 (2013) 6746–6748.

[24] Z. Bie, W. Zhao, Z. Lv, S. Liu, Y. Chen, Preparation of salbutamol imprinted magnetic nanoparticles via boronate affinity oriented surface imprinting for the selective analysis of trace salbutamol residues, Analyst 144 (2019) 3128–3135.
[25] D. Li, Z. Bie, F. Wang, E. Guo, fficient synthesis of riboflavin-imprinted magnetic nanoparticles by boronate affinity-based surface imprinting for the selective recognition of riboflavin, Analyst 143 (2018) 4936–4943.
[26] D. Li, T. Tu, M. Yang, C. Xu, Efficient preparation of surface imprinted magnetic nanoparticles using poly(2-anilinoethanol) as imprinting coating for the selective recognition of glycoprotein, Talanta 184 (2018) 316–324.
[27] D. Li, T. Tu, X. Wu, Efficient preparation of template immobilization-based boronate affinity surface-imprinted silica nanoparticles using poly(4-aminobenzyl alcohol) as an imprinting coating for glycoprotein recognition, Anal. Methods 10 (2018) 4419–4429.
[28] L. Chen, X. Wang, W. Lu, X. Wu, J. Li, Molecular imprinting: perspectives and applications, Chem. Soc. Rev. 45 (2016) 2137–2211.
[29] J. Yu, X. Wang, Q. Kang, J. Li, D. Shen, L. Chen, One-pot synthesis of a quantum dot-based molecular imprinting nanosensor for highly selective and sensitive fluorescence detection of 4-nitrophenol in environmental waters, Environ. Sci. Nano. 4 (2017) 493–502.
[30] X. Wang, S. Yu, J. Wang, J. Yu, M. Arabi, L. Fu, B. Li, J. Li, L. Chen, Fluorescent nanosensor designing via hybrid of carbon dots and post-imprinted polymers for the detection of ovalbumin, Talanta 211 (2020), 120727.
[31] Q. Yang, C. Li, J. Li, X. Wang, M. Arabi, H. Peng, H. Xiong, L. Chen, Rational construction of a triple emission molecular imprinting sensor for accurate naked-eye detection of folic acid, Nanoscale 12 (2020) 6529–6536.
[32] Q. Yang, J. Li, X. Wang, H. Xiong, L. Chen, Ternary emission of a blue-, green-, and red-based molecular imprinting fluorescence sensor for the multiplexed and visual detection of bovine hemoglobin, Anal. Chem. 91 (2019) 6561–6568.
[33] J. Li, J. Fu, Q. Yang, L. Wang, X. Wang, L. Chen, Thermosensitive molecularly imprinted core–shell CdTe quantum dots as a ratiometric fluorescence nanosensor for phycocyanin recognition and detection in seawater, Analyst 143 (2018) 3570–3578.
[34] X. Wang, S. Yu, W. Liu, L. Fu, Y. Wang, J. Li, L. Chen, Molecular imprinting based hybrid ratiometric fluorescence sensor for the visual determination of bovine Hemoglobin, ACS Sens. 3 (2018) 378–385.
[35] B. Li, Z. Zhang, J. Qi, N. Zhou, S. Qin, J. Choo, L. Chen, Quantum dot-based molecularly imprinted polymers on three-dimensional origami paper microfluidic chip for fluorescence detection of phycocyanin, ACS Sens. 2 (2017) 243–250.
[36] X. Wang, J. Yu, X. Wu, J. Fu, Q. Kang, D. Shen, J. Li, L. Chen, A molecular imprinting-based turn-on Ratiometric fluorescence sensor for highly selective and sensitive detection of 2,4-dichlorophenoxyacetic acid (2,4-D), Biosens. Bioelectron. 81 (2016) 438–444.
[37] S. Wang, D. Yin, W. Wang, X. Shen, J.J. Zhu, H.Y. Chen, Z. Liu, Targeting and imaging of cancer cells via monosaccharide-imprinted fluorescent nanoparticles, Sci. Rep. 6 (2016) 22757.
[38] E. Cazares-Cortes, M. Nerantzaki, J. Fresnais, C. Wilhelm, N. Griffete, C. Ménager, Magnetic nanoparticles create hot spots in polymer matrix for controlled drug release, Nanomaterials 8 (2018) 850.
[39] Y. Yang, H. Niu, H. Zhang, Direct and highly selective drug optosensing in real, undiluted biological samples with quantum-dot-labeled hydrophilic molecularly imprinted polymer microparticles, ACS Appl. Mater. Interfaces 8 (2016) 15741–15749.
[40] D. Li, N. Wang, F. Wang, Q. Zhao, Boronate affinity-based surface-imprinted quantum dots as novel fluorescent nanosensors for the rapid and efficient detection of rutin, Anal. Methods 11 (2019) 3212–3220.
[41] D. Li, S. Zhai, R. Song, Z. Liu, Determination of cis-diol-containing flavonoids in real samples using boronate affinity quantum dots coated with imprinted silica based on controllable oriented surface imprinting approach, Spectrochim. Acta A Mol. Biomol. Spectrosc. 227 (2020), 117542.
[42] Y. Zhang, S. Li, X.T. Ma, X.W. He, W.Y. Li, Y.K. Zhang, Carbon dots-embedded epitope imprinted polymer for targeted fluorescence imaging of cervical cancer via recognition of epidermal growth factor receptor, Microchim. Acta 187 (2020) 228.
[43] D. Yin, X. Li, Y. Ma, Z. Liu, Targeted cancer imaging and photothermal therapy via monosaccharide-imprinted gold nanorods, Chem. Commun. 53 (2017) 6716–6719.
[44] S. Beyazit, B. Tse Sum Bui, K. Haupt, C. Gonzato, Molecularly imprinted polymer nanomaterials and nanocomposites by controlled/living radical polymerization, Prog. Polym. Sci. 62 (2016) 1–21.
[45] Y. Ma, S. Xu, S. Wang, L. Wang, Luminescent molecularly-imprinted polymer nanocomposites for sensitive detection, Trac-Trend Anal. Chem. 67 (2015) 209–216.
[46] Q. Yang, J. Li, X. Wang, H. Peng, H. Xiong, L. Chen, Strategies of molecular imprinting-based fluorescence sensors for chemical and biological analysis, Biosens. Bioelectron. 112 (2018) 54–71.
[47] S. Silvi, A. Credi, Luminescent sensors based on quantum dot–molecule conjugates, Chem. Soc. Rev. 44 (2015) 4275–4289.
[48] O. Adegoke, N. Nic Daeid, Alloyed AuFeZnSe quantum dots@gold nanorod nanocomposite as an ultrasensitive and selective plasmon-amplified fluorescence OFF-ON aptasensor for arsenic (III), J. Photochem. Photobiol. A: Chem. 426 (2022), 113755.
[49] Q. Ma, X. Su, Near-infrared quantum dots: synthesis, functionalization and analytical applications, Analyst 135 (2010) 1867–1877.
[50] L.M. Armijo, Y.I. Brandt, D. Mathew, S. Yadav, S. Maestas, A.C. Rivera, N.C. Cook, N.J. Withers, G.A. Smolyakov, N.L. Adolphi, T.C. Monson, D.L. Huber, H.D. C. Smyth, M. Osiński, Iron oxide nanocrystals for magnetic hyperthermia applications, Nanomaterials 2 (2012) 134–146.
[51] O. Adegoke, K. Takemura, E.Y. Park, Plasmonic oleylamine-capped gold and silver nanoparticle-assisted synthesis of luminescent alloyed CdZnSeS quantum dots, ACS Omega 3 (2018) 1357–1366.
[52] J. Bai, L. Chen, Y. Zhu, X. Wang, X. Wu, Y. Fu, A novel luminescence sensor based on porous molecularly imprinted polymer-ZnS quantum dots for selective recognition of paclitaxel, Colloids Surf. A Physicochem. Eng. Asp. 610 (2021), 125696.
[53] S. You, A.-Q. Luo, D. Biswal, J.Z. Hilt, D.A. Puleo, Lysozyme-imprinted polymer synthesized using UV free-radical polymerization, Talanta 83 (2010) 156–161.
[54] Y. Volkov, Quantum dots in nanomedicine: recent trends, advances and unresolved issues, Biochem. Biophys. Res. Commun. 468 (2015) 419–427.
[55] Y. Luo, Y. Wang, M. Liu, H. Zhu, O. Chen, S. Zuo, J. Zhao, Colloidal assembly of Au−quantum dot−Au sandwiched nanostructures with strong plasmon−exciton coupling, J. Phys. Chem. Lett. 11 (2020) 2449–2456.
[56] N. Al-Salim, A.G. Yung, R.D. Tilley, A.J. McQuillan, J. Xia, Synthesis of CdSeS nanocrystals in coordinating and noncoordinating solvents: solvent's role in evolution of the optical and structural properties, Chem. Mater. 19 (2007) 5185–5193.
[57] A.M. Smith, S. Nie, Minimizing the hydrodynamic size of quantum dots with multifunctional multidentate polymer ligands, J. Am. Chem. Soc. 130 (2008) 11278–11279.
[58] R.L. Penn, J.F. Banfield, Oriented attachment and growth, twinning, polytypism, and formation of metastable phases: Insights from nanocrystalline TiO_2, Am. Mineral. 83 (1998) 1077–1082.
[59] L. Roach, S. Ye, S.C.T. Moorcroft, K. Critchley, P.L. Coletta, S.D. Evans, Morphological control of seedlessly-synthesized gold nanorods using binary surfactants, Nanotechnology 29 (2018), 135601.
[60] S. Biswas, P. Tripathi, N. Kumar, S. Nara, Gold nanorods as peroxidase mimetics and its application for colorimetric biosensing of malathion, Sens. Actuators B Chem. 231 (2016) 584–592.
[61] E. Rafiee, S. Shahebrahimi, M. Feyzi, M. Shaterzadeh, Optimization of synthesis and characterization of nanosilica produced from rice husk (a common waste material), Int. Nano Lett. 2 (2012) 29.
[62] S. Chen, Y. Li, S. Wu, X. Jiang, H. Yang, X. Su, L. He, L. Zou, X. Ao, S. Liu, Y. Yang, A phosphorescent probe for cephalexin consisting of mesoporous thioglycolic acid-modified Mn:ZnS quantum dots coated with a molecularly imprinted polymer, Microchim. Acta 187 (2020) 40.
[63] O. Adegoke, H. Montaseri, S.A. Nsibande, P.B.C. Forbes, Passivating effect of ternary alloyed AgZnSe shell layer on the structural and luminescent properties of CdS quantum dots, Mater. Sci. Semicond. Process. 90 (2019) 162–170.
[64] A.F.E. Hezinger, J. Teßmar, A. Göpferich, Polymer coating of quantum dots – A powerful tool toward diagnostics and sensorics, Eur. J. Pharm. Biopharm. 68 (2008) 138–152.
[65] F.-C. Gong, D.-X. Wu, Z. Cao, X.-C. He, A fluorescence enhancement-based sensor using glycosylated metalloporphyrin as a recognition element for levamisole assay, Biosens. Bioelectron. 22 (2006) 423–428.
[66] Th.F. Vandamme, M. Demoustier, B. Rollmann, Quantitation of levamisole in plasma using high performance liquid chromatography, Eur. J. Drug Metab. Pharmacokinet. 20 (1995) 145–149.
[67] S. Marriner, E.A. Galbraith, J.A. Bogan, Determination of the anthelmintic levamisole in plasma and gastro-intestinal fluids by high-performance liquid chromatography, Analyst 105 (1980) 993–996.
[68] S. Sowjanya, Ch Devadasu, Development of RP-HPLC method for the simultaneous quantitation of levamisole and albendazole: application to assay validation, Int. J. Anal. Chem. (2018) 9. Article ID 5746305.